Journal of Materials Chemistry A

ROYAL SOCIETY OF CHEMISTRY

PAPER

View Article Online
View Journal | View Issue

Cite this: J. Mater. Chem. A, 2025, 13, 4452

Facilitating polysulfide conversion kinetics *via* multifunctional solid-state electrolytes under lean electrolyte conditions for lithium–sulfur batteries†

Hyunji Park,[a] Jooyoung Lee[a] and Choongho Yu *[ab]

Received 26th October 2024
Accepted 28th December 2024

DOI: 10.1039/d4ta07639g

rsc.li/materials-a

The sluggish redox kinetics of polysulfides under lean electrolyte conditions hinder practical applications of lithium–sulfur batteries. Herein, a polar solid-state electrolyte, $Li_{10}GeP_2S_{12}$ (LGPS) whose ionic conductivity is higher than that of highly concentrated polysulfide electrolytes (or catholytes), could greatly alleviate the problem by providing pathways for lithium ions and attracting polysulfides to facilitate the conversion reactions. The affinity of polysulfides to LGPS and the catalytic effect enhancing kinetics were confirmed by density functional theory calculations and experimental results mainly from cyclic voltammetry and potentiostatic discharge. The LGPS inclusion in the cathode has significantly improved the performances of the cells showing a high areal capacity of 6.13 mA h cm^{-2} with an outstanding retention (70% at the 135th cycle) despite the extremely low electrolyte-to-sulfur ratio (E/S ratio of 2.9 μL mg^{-1}), a high sulfur loading of 8.1 mg cm^{-2}, and a low ratio of anode to cathode capacity (N/P ratio of 2). Further research and development could pave the way for practical and efficient energy storage solutions using multifunctional solid-state electrolyte approaches.

Introduction

Lithium–sulfur (Li–S) batteries have garnered significant attention as next-generation alternatives to lithium-ion (Li-ion) batteries due to their remarkable theoretical specific capacity of 1675 mA h g^{-1} and exceptionally high energy density of 2567 W h kg^{-1}.[1] Furthermore, sulfur offers several advantages as a cathode active material, including abundance, low cost, and environmental friendliness.[2] Unlike Li-ion batteries, which operate based on an intercalation mechanism, Li–S batteries function through electrochemical redox conversion. During the discharge process, solid sulfur (S_8) in the cathode becomes soluble polysulfide intermediates, such as Li_2S_x ($4 \leq x \leq 6$).[3] Then, a liquid–solid phase transition occurs resulting in solid discharge products such as Li_2S. Due to the multi-phase conversion reactions, Li–S batteries suffer from sluggish kinetics due to the increased viscosity of the soluble polysulfides in the electrolyte as well as the polysulfide shuttling causing side reactions with the lithium metal anode.[4] In addition, it is necessary to have thin and uniform depositions of the solid products, such as S_8 and Li_2S due to their insulating properties.[5,6]

The undesirable results from the aforementioned shuttling have been greatly attenuated by various recent studies including functional separators,[7–9] graphene composite separators,[10] and artificial solid-electrolyte interphase (SEI) layers on lithium anodes to avoid direct contact of polysulfides with lithium metal.[11–13] To avoid thick and non-uniform deposition of the solid products, porous structures with large surface areas were employed such as porous carbon nanotubes[14–17] and functional groups to attract polysulfides on the host surface.[18,19]

Despite the recent progress, Li–S batteries are yet to be attractive in practice, particularly due to the low energy density under flooded electrolyte conditions and low sulfur loadings in most of the literature studies. Considering the commercial Li-ion batteries, the electrolyte/sulfur (E/S) ratio needs to be lower than 3 μL mg^{-1} with sulfur loadings higher than ~5 mg cm^{-2}.[20,21] Such lean electrolyte conditions induce low sulfur utilization, large polarization, and low ionic conductivity due to the increased viscosity of electrolyte. Recent studies attempted interesting approaches including the various cathode structures,[22–27] electrolyte components,[28–32] and binders.[33] A noticeable approach is facilitating polysulfide conversion reactions by electrocatalysts or promoters.[4,5,34] For example, Mn-based catalysts were tested with a low E/S ratio of 4.6 μL mg^{-1} with a high sulfur loading of 5.6 mg cm^{-2}.[35] However, under ultra-lean electrolyte conditions corresponding to an E/S ratio of 3 μL mg^{-1}, most studies have only demonstrated feasibility, and there are few papers reporting operation beyond 100 cycles under these conditions. Lean-electrolyte Li–S batteries not only show an overall low capacity, but particularly make the Li_2S nucleation process difficult,

[a]Department of Mechanical Engineering, Texas A&M University, College Station, Texas 77843, USA. E-mail: chyu@tamu.edu

[b]Department of Materials Science and Engineering, Texas A&M University, College Station, Texas 77843, USA

† Electronic supplementary information (ESI) available. See DOI: https://doi.org/10.1039/d4ta07639g

deepening the Li_2S nucleation dip at the point where the second discharge plateau begins due to the overpotential. Research has been conducted to investigate the origin of the increased overpotential under lean electrolyte conditions, which can be divided into three factors: (1) interfacial charge transfer, (2) polysulfide diffusion, and (3) ion conduction.[36,37] Electrochemical impedance spectroscopy-galvanostatic intermittent titration technique (EIS-GITT) analysis has demonstrated that interfacial charge transfer is the kinetic limiting factor in lean electrolyte Li–S batteries.[37,38] However, the proportion of this overpotential varies depending on the solvent used, salt concentration, type of anion, depth of discharge and E/S ratio, and the proportion of overpotential caused by polysulfide diffusion and ionic conduction is also significant. Therefore, the influence of polysulfide diffusion and ion conduction cannot be ignored,[39–41] and we need a comprehensive solution that is not focused on just one factor. Another challenge for practical Li–S batteries is the ratio of anode to cathode capacity (so-called N/P ratio) as the literature often shows results with unlimited supply of lithium. At low N/P ratios, limited lithium sources cause considerable capacity fading due to the side reactions of lithium with polysulfides. It was found that the N/P ratio needs to be smaller than 3 to realize the high energy density of Li–S batteries.[42,43]

This study introduces a solid-state electrolyte, $Li_{10}GeP_2S_{12}$ (LGPS) superionic conductor whose Li-ion conductivity is 10^{-2} S cm^{-1} or higher,[44] as an additive to promote kinetics of lean-electrolyte Li–S batteries. Due to its high ionic conductivity, LGPS has been reported as an electrolyte in solid-state lithium–sulfur batteries. LGPS could provide a Li-ion transporting pathway in highly concentrated catholytes (or polysulfide electrolytes) whose ionic conductivity is considerably lowered, facilitating liquid/solid polysulfide conversion reactions. The affinity of polysulfides to polar LGPS, as confirmed by the density functional theory (DFT) calculation, assists the multi-phase reactions and the catalytic effect promotes kinetics as presented in the cyclic voltammetry, potentiostatic discharge and electrochemical impedance spectroscopy (EIS) results. Specifically, we observed an increase in the Li_2S nucleation dip voltage, confirming that it significantly contributed to the liquid/solid conversion process. Alleviating concerns about the limited compatibility of sulfide solid electrolytes with solvents, it was confirmed that LGPS remains stable in ether-based electrolytes without showing a decrease in ionic conductivity or other side effects, as evidenced by cycling tests, EIS, UV-vis spectroscopy, and color change observations. The addition of LGPS in the cathode led to a high areal capacity of 6.13 mA h cm^{-2} with outstanding retention (70% at the 135th cycle) under lean electrolyte conditions (E/S ratio of 2.9 μL mg^{-1}) despite a high sulfur loading of 8.1 mg cm^{-2} and a low N/P ratio of 2.

Results and discussion

LGPS as a lithium transport pathway and polysulfide immobilizer

Under lean electrolyte conditions with low E/S ratios, the catholyte becomes viscous due to the increased polysulfide concentration, which diminishes its ionic conductivity,[16] resulting in sluggish kinetics. As shown in Fig. 1b, the ionic conductivity is inversely proportional to the sulfur concentration. For a typical E/S ratio of 15 μL mg^{-1} in the literature,[45] the polysulfide concentration and conductivity are respectively ~2 M and 6.6 mS cm^{-1} in an ether-based electrolyte[16] while a lean electrolyte condition of ~5 μL mg^{-1} (~6 M) significantly decreases the conductivity to 2.30 mS cm^{-1}. When the catholyte is more concentrated to the solubility limit level (~8 M catholyte),[29,46,47] the ionic conductivity is further reduced to 1.05 mS cm^{-1}. Considering the relatively high conductivity of ~10 mS cm^{-1} for conventional Li-ion batteries, such a low conductivity significantly reduces the kinetics of Li ions, leading to poor rate capability and severe side reactions.

LGPS is a solid-state electrolyte whose conductivity is comparable to those of conventional liquid electrolytes. The diameter of the LGPS particles ranges from hundreds of nanometers to several microns, as shown in Fig. S1.† The high ionic conductivity of LGPS can be attributed to the fast diffusion of lithium ions with one-dimensional diffusion pathways along the *c* axis in its unique structure, including LiS_6 octahedra and $(Ge_{0.5}P_{0.5})S_4$ tetrahedra.[44] The ionic conductivity (2–5 mS cm^{-1}) of LGPS is higher than those of lean polysulfide electrolytes, suggesting that LGPS could be effective in transporting Li-ions (Fig. 1a). In particular, the concentration of polysulfides increases near the CNTs where polysulfide redox reactions occur as the CNTs are the main conduits for electron transfer. More specifically, the conversion from solid-state S_8 to liquid-state Li_2S_6 (during discharge) and from solid-state Li_2S to liquid-state Li_2S_6 (during charge) makes the polysulfide concentration near the CNTs high, resulting in sluggish Li-ion transport limiting further reactions. Here the invariant conductivity of LGPS would provide better Li-ion diffusion pathways and the affinity of polysulfides could noticeably improve the reaction kinetics.

The cathode was fabricated by sandwiching the LGPS powders between two slices of the CNT layer (Fig. 1a). The porous CNT layer allowed the catholyte to be smeared, serving as a host for the polysulfides.[16] After the formation process with the liquid catholyte, the LGPS powders dispersed because they are small enough to be spread in the CNT layer whose pores are several microns in size (Fig. 1c, S1 and S2†). Even though LGPS was originally placed between two CNT layers, these particles were found on the outer surface of the sandwiched electrode after cycling (Fig. 1c and S6†). In the meantime, the CNTs were mechano-chemically treated to create trenches on their walls with polysulfide–philic carboxylic groups.[18] Thus, the synergistic effect of the functionalized CNTs and LGPS would facilitate the redox kinetics of lithium polysulfides particularly under lean electrolyte conditions. In our experiment, sandwiching LGPS between two CNT layers was more effective than incorporating LGPS into the CNT layer using a wet slurry coating method because LGPS more or less reacted with conventional solvents such as *N*-methylpyrrolidone, reducing ionic conductivity and thereby lowering sulfur utilization and specific capacity[48] (Fig. S4 and 5†).

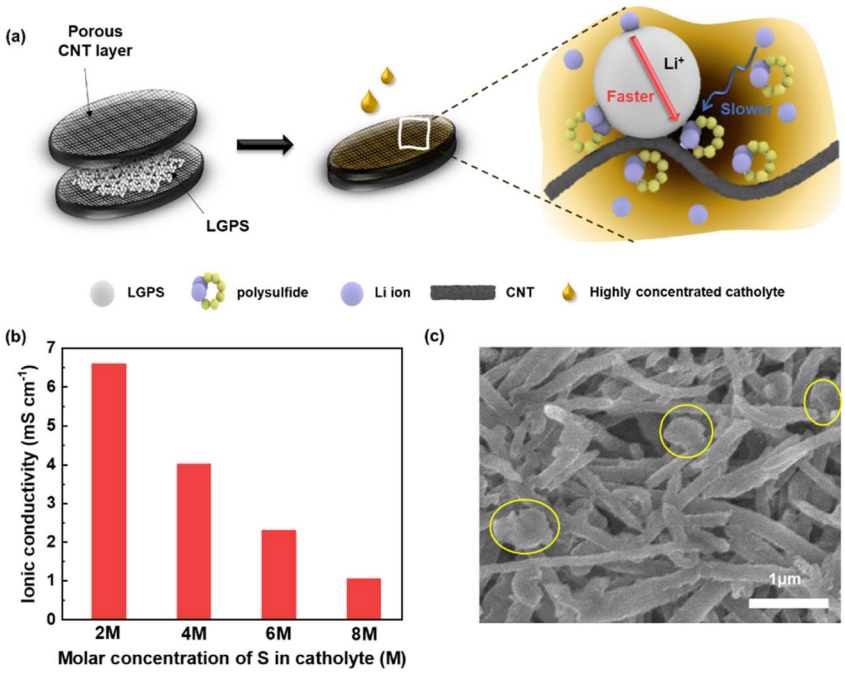

Fig. 1 (a) The cathode was fabricated by sandwiching LGPS particles, followed by the application of a polysulfide solution onto the porous structure. While lithium ions are readily transported through LGPS, their movement is sluggish through the lean polysulfide electrolyte. (b) The ionic conductivity of 2 M, 4 M, 6 M and 8 M catholyte. (c) The scanning electron microscopy (SEM) image of a CNT/LGPS electrode with distributed LGPS particles after cycling.

To understand the interactions between LGPS and polysulfides, various adsorption configurations and corresponding energies were calculated by DFT (Fig. 2, S7–S9 and Tables S1–S3†). The adsorption energy (E_{ads}) between the polysulfides and LGPS (labeled as a substrate) was calculated using the following formula.

$$E_{ads} = E_{total} - E_{substrate} - E_{PS} \quad (1)$$

where E_{total} is the energy of the optimized configuration with lithium polysulfides adsorbed, and $E_{substrate}$ and E_{PS} are the energies of the pristine substrate and isolated lithium polysulfides. For comparison, graphitic carbon as a substrate was also evaluated. All the polysulfide intermediates (Li_2S_n, $n = 8$, 6, 4, 2, 1) and S_8 on the LGPS (001) surface were examined (Fig. 2a). According to the literature, the diffusion of Li ions is mainly along the [001] direction.[44,49,50] Thus, we used the LGPS (001) surface to calculate the interaction between LGPS and polysulfides. Compared to graphitic carbon, the LGPS (001) surface showed stronger adhesion towards polysulfides with lower adsorption energies of −1.18, −1.11, −0.88, −1.17, −1.40, and −1.96 eV for S_8, Li_2S_8, Li_2S_6, Li_2S_4, Li_2S_2, and Li_2S, respectively. On the other hand, those of the graphitic carbon were higher, which are −0.04, −0.07, −0.84, −0.46, −0.16, and −0.23 eV for S_8, Li_2S_8, Li_2S_6, Li_2S_4, Li_2S_2, and Li_2S, respectively (Fig. 2c). The adsorption energies of S_8 and Li_2S_8 with graphitic carbon are close to zero. While LGPS formed bonding with polysulfides whose lengths are 2.3–2.5 Å (Fig. S9†), the graphitic carbon substrate does not appear to form a bond with polysulfides. This clearly indicates that the polarity of LGPS plays a crucial role in polysulfide adsorption. As shown in Fig. 1a, it is observed that Li_2S_6 and Li_2S_8 create more intricate bonding arrangements with LGPS. In Li_2S_6, the sulfur and lithium atoms form bonds with the lithium and sulfur atoms in LGPS, respectively. Notably, the sulfur atom of Li_2S_6 bonds with two lithium atoms of LGPS. Li_2S_8 exhibits a comparable bonding pattern but with an asymmetrical arrangement. In addition, a visualized adsorption experiment of LGPS was carried out with polysulfides using a 5 mM Li_2S_6 solution (Fig. 2d). When 20 mg LGPS was added to 3 mL of the polysulfide solution, the reddish color of the solution became greenish, and the corresponding ultraviolet-visible (UV-vis) spectra show significant reductions in the absorbance peaks corresponding to the polysulfides. This experiment also shows that LGPS does not decompose in the catholyte based on 1,3-dioxolane (DOL) and 1,2-dimethoxyethane (DME). In contrast, in the case of other polar solvents, new peaks generated by decomposition were observed in the UV/vis spectra, but this was not the case with our catholyte.[48] In polar solvents, the addition of LGPS indicates chemical decomposition and a significant decrease in ionic conductivity, as evidenced by the solution turning blue.[48] The color change of the solvent can be used as an indirect indicator of LGPS degradation. However, in 1M LiTFSI in DOL/DME electrolyte, no color change or dissolution was observed even after a day (Fig. S11†). The stability of LGPS in ether-based electrolytes has been reported in several studies through unchanged X-ray diffraction (XRD) patterns and ionic conductivity.[51,52] Wan *et al.* demonstrated the compatibility of LGPS with ether-based solvents by reporting a solid–liquid hybrid electrolyte using LGPS with

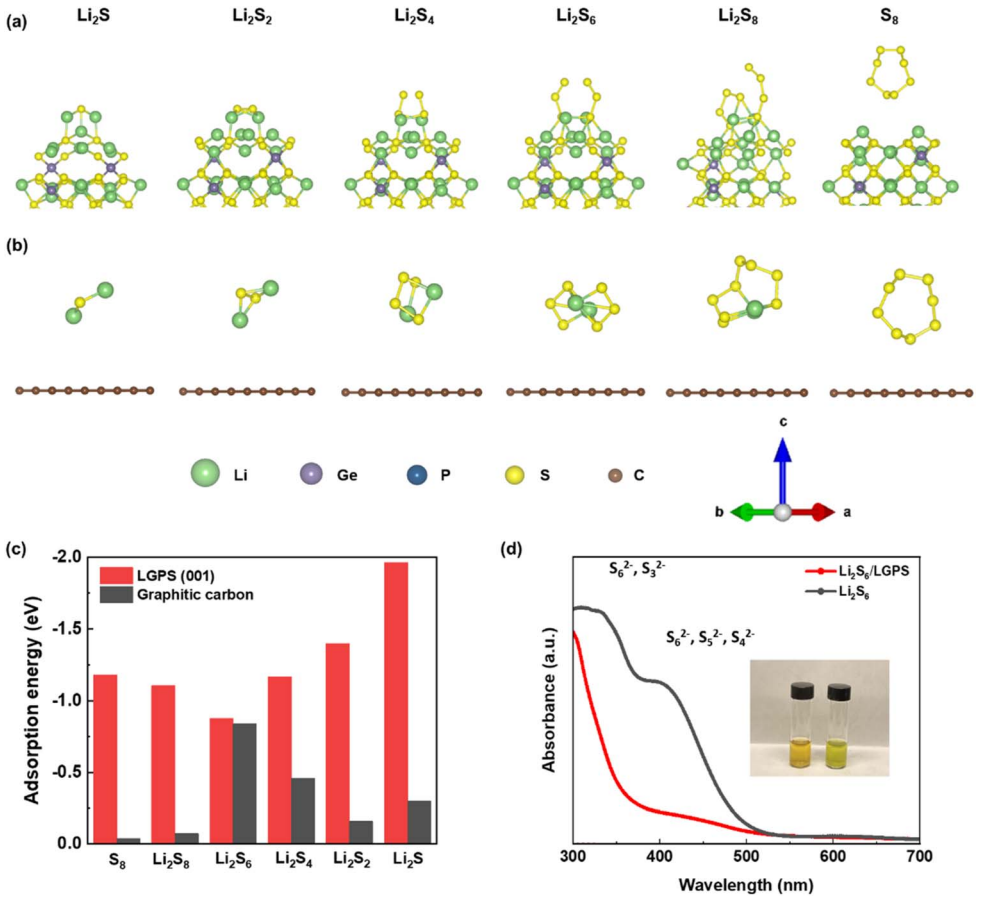

Fig. 2 The adsorption configuration of lithium polysulfides and S_8 on (a) LGPS (001) and (b) graphitic carbon. (c) Adsorption energies of lithium polysulfides on LGPS and graphitic carbon. (d) UV-vis spectra of a 5 mM Li_2S_6 solution before (black line; left photo inset) and after (red line; right photo inset) immersion of LGPS in the solution.

LiTFSI–$Mg(TFSI)_2$ in DME.[53] To evaluate the stability of LGPS in a highly concentrated catholyte, we mixed 100 mg of LGPS with 2 mL of 6M catholyte (Fig. S12†). After two days, the catholyte was washed off, and the LGPS precipitates were separated from the catholyte. The whitish LGPS appeared to be the same as the original powders, as shown in Fig. S12(c).† XRD measurements further confirmed that LGPS remained stable throughout the experiment, as displayed in Fig. S13.†

Kinetic effects of LGPS in the cathode

To investigate the kinetic effects of LGPS in the cathode, cyclic voltammetry (CV) and potentiostatic discharge experiments were performed using two different CNT cathodes with and without LGPS. As shown in Fig. 3a, S_8 was reduced to Li_2S_n (C1) at around 2.1–2.3 V *vs.* Li^+/Li and to Li_2S (C2) at around 1.8–2.0 V *vs.* Li^+/Li. Two anodic peaks are attributed to the oxidation process of Li_2S to short-chain polysulfide (A1) and further oxidation to S (A2). Compared with the electrode without LGPS, the reduction peaks of CNT/LGPS shifted positively, while its oxidation peaks moved negatively, indicating that LGPS can reduce electrochemical polarization with enhanced redox reaction kinetics. In addition, CNT/LGPS exhibits sharper peaks with increased current density, which is related to the Tafel slope and the diffusion coefficient. The Tafel slopes for the cathodic CV peaks of C1 and C2 are displayed in Fig. 3b. As for the C1 peak, the addition of LGPS leads to a smaller Tafel slope (165.6 mV dec^{-1}) than that of CNTs only (233.5 mV dec^{-1}). Similarly, the Tafel slopes of the C2 peak were 208.2 and 318.4 mV dec^{-1} respectively for the cathodes with and without LGPS. This implies that LGPS effectively accelerates the reduction of polysulfides.

Based on the Tafel slope, the relative activation energies were calculated by using the following equation.[54–58]

$$E_a = E_a^0 - \frac{RT}{b}\varphi \quad (2)$$

where E_a is the activation energy of the reduction process; E_a^0 is the intrinsic activation energy; φ is the peak potential of the reduction process in the CV curve; b is the slope of the Tafel plot; R is the gas constant; T is the absolute temperature (see details in Note S1, ESI†). Using the relationship between the electrode potential, the Tafel equation, and activation energy, the difference in activation energy between CNT/LGPS and CNTs can be estimated. The activation energy of CNT/LGPS for the reduction of elemental sulfur to long-chain polysulfides was reduced by 10.8 kJ mol^{-1} compared to that of CNTs. For the

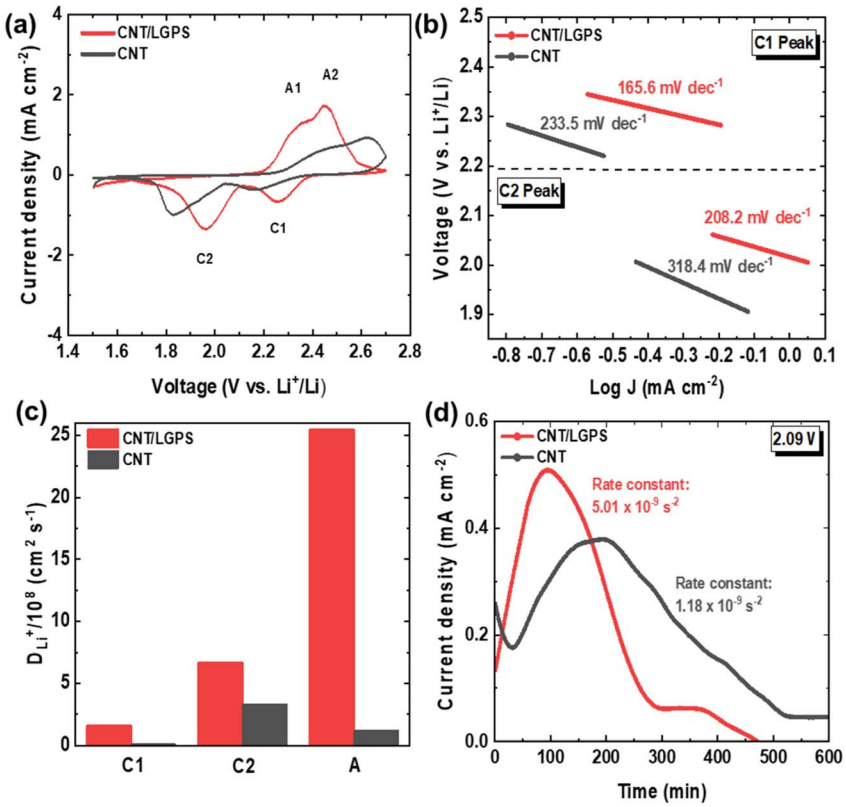

Fig. 3 (a) The CV profiles of the cathodes with and without LGPS at a scan rate of 0.02 mV s^{-1}. (b) Tafel plots corresponding to the reductions of elemental sulfur to Li_2Sn (upper) and Li_2Sn to Li_2S (lower). *J* is the current density in 'a'. (c) The diffusion coefficients of Li-ions corresponding to C1, C2, and A in the CV results. (d) Potentiostatic discharge curves at 2.09 V to initiate the nucleation and growth of Li_2S.

reduction of long-chain polysulfides to short-chain polysulfides, the activation energy of CNT/LGPS was decreased by 9.1 kJ mol^{-1} compared to that of the CNT cathode without LGPS. This implies that LGPS exhibits a catalytic effect, reducing the activation energy and promoting reaction kinetics.

We also found the diffusion coefficient (D) of Li-ions using the Randles–Sevcik equation whose parameters were found from the CV cycles at scan rates of 0.03–0.05 mV s^{-1} (Fig. 3c, S14–16 and Table S4†).

$$i_p = 0.4463nFAC\left(\frac{nFvD}{RT}\right)^{\frac{1}{2}} \quad (3)$$

where i_p is the peak current; n is the number of electrons transferred; A is the electrode area; C is the concentration of Li-ions; F is the Faraday constant; v is the scan rate of voltage. The diffusion coefficients of Li-ions in the cathode with LGPS are higher than those without LGPS. It appears that the Li-ion diffusion (C2) through the lean catholyte during the discharge reactions covering the major portion of the capacity has been doubled. At a low scan rate of 0.02 mV s^{-1}, the anodic peak appears as two distinct peaks, but as the scan rate increases, they merge into a single peak (Fig. S15†). Therefore, when calculating the diffusion coefficient, the combined A peak was used instead of separating it into A1 and A2 peaks. During the charge process, Li^+ diffusion has greatly increased, suggesting that the liquid–solid conversion can be improved.

The influence of LGPS on Li_2S nucleation and growth was identified by potentiostatic discharge experiments (Fig. 3d) with the following equations, calculating the effective rate constant for the coverage of the carbon host surface by Li_2S, $N_0\kappa^2$.[59–61]

$$\frac{J}{J_m} = \left(\frac{t}{t_m}\right)\exp\left[-\frac{1}{2}\left(\frac{t^2}{t_m{}^2} - 1\right)\right] \quad (4)$$

where J and t represent the current density and time, respectively; and the subscript m indicates their maximum current and the corresponding time values.

$$t_m = \left(2\pi N_0\kappa^2\right)^{-\frac{1}{2}} \quad (5)$$

where N_0 represents the areal density of Li_2S nuclei; κ gives the rate constant of lateral growth of Li_2S. It was found that LGPS accelerates Li_2S nucleation with a higher rate constant of 5.01×10^{-9} S^{-2} at 2.09 V, which is more than four times higher than that of the cathode without LGPS (1.18×10^{-9} S^{-2}).

Electrochemical performances of lean Li–S batteries

The cell performances with LGPS (E/S ratio of 7.8 μL mg^{-1}) were tested with 4 M catholyte. The addition of LGPS to the cathode increased the specific capacity from 1099 mA h g^{-1} to 1172 mA h g^{-1} after two activation cycles at 0.2C (Fig. S18†).

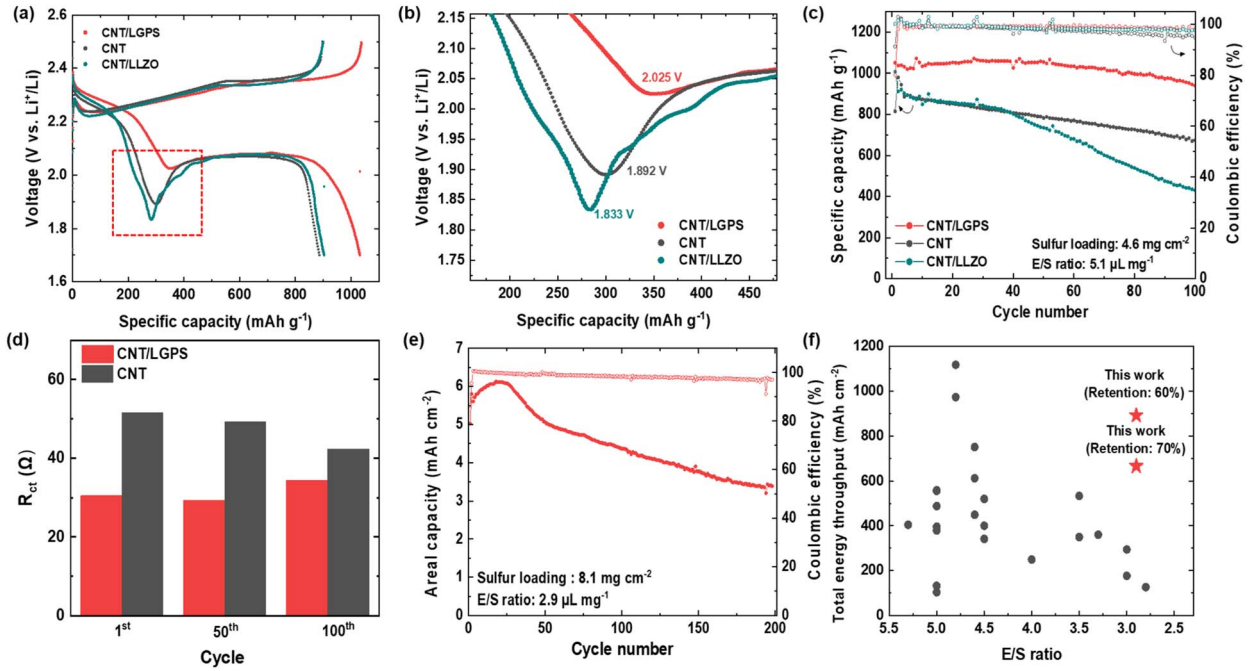

Fig. 4 (a) Representative galvanostatic charge/discharge profiles of the cells with LGPS or LLZO and without the solid-state electrolyte at 0.1C with a sulfur loading of 4.6 mg cm^{-2} and E/S ratio of 5.1 μL mg^{-1}. (b) Enlarged profiles marked with a square in 'a'. (c) The cycling performances of the three cases at 0.1C, showing the outperforming case from the CNT/LGPS cell. (d) The comparison of the charge transfer resistance with and without LGPS at the 1st, 50th, and 100th cycles. (e) The areal capacity of the LGPS cell at 0.05C with a high sulfur loading of 8.1 mg cm^{-2} under very lean electrolyte conditions (E/S ratio of 2.9 μL mg^{-1}). (f) The total energy throughputs over the course of the cycles at the 135th and 200th cycles (capacity retention of 70% and 60%, respectively) as a function of the E/S ratio along with those in the literature with sulfur loadings of 4 mg cm^{-2} and higher.

Furthermore, the rate capability was consistent with the kinetics study that LGPS further improved kinetics of the cathode (Fig. S18–S20†). The LGPS-containing cell showed 1187 mA h g^{-1} at 0.8C, but the capacity without LGPS was very small, indicating sluggish polysulfide conversion kinetics. When the E/S ratio was 7.8 μL mg^{-1}, LGPS enhanced sulfur utilization and improved rate capability. However, the nucleation barrier of Li_2S may not be substantially beneficial because the ionic conductivity of the 4 M catholyte (~7.8 μL mg^{-1}) is similar to that of LGPS. As the E/S ratio further decreases, the kinetics of nucleation and growth of Li_2S become more sluggish with lowered ionic conductivity, posing a significant challenge. In this context, the relatively higher ionic conductivity of LGPS under leaner electrolyte conditions is more effective in boosting the kinetics.

To assess the influence of the relatively high ionic conductivity of LGPS compared to that of the polysulfide electrolyte, we tested Ta-doped $Li_{6.4}La_3Zr_{1.4}Ta_{0.6}O_{12}$ (LLZO) solid-state electrolyte, which has a lower ionic conductivity than LGPS, under lean electrolyte conditions (E/S ratio of 5.1 μL mg^{-1}) with 6 M polysulfides (molarity is based on S rather than Li_2S_6). Since the ionic conductivity of LLZO is 0.1–1 mS cm^{-1},[62,63] which is lower than those of liquid electrolytes, it would play a smaller role in transporting lithium ions. As shown in Fig. 4a, the CNT/LGPS cell shows higher specific capacity compared to CNTs and CNT/LLZO cells. The CNT/LGPS cell displayed a high initial specific capacity of 1038 mA h g^{-1} with a capacity retention of 91% at the 100th cycle (Fig. 4c). In contrast, the addition of LLZO did not improve the capacity of the reference cell using only the CNT electrode. The more rapid capacity fading with LLZO suggests that the inferior ion conduction through LLZO may have hindered Li-ion transport and the diffusion of polysulfides. A noticeable difference with the addition of LGPS was the discharge voltage profile at the nucleation dip of Li_2S (Fig. 4a and b). The nucleation voltage was increased with LGPS (2.025 V *vs.* Li^+/Li) from 1.892 V, lowering the overpotential of liquid–solid conversion. The rate capability results (Fig. S21†) indicate that LGPS promotes reaction kinetics showing a capacity of 889 mA h g^{-1} at 0.3C where the capacity is close to zero without LGPS. A two times higher LGPS loading (3 mg cm^{-2}, 40 wt%) did not noticeably increase the specific capacity compared to the case of 1.5 mg cm^{-2} (Fig. S22†), suggesting that polysulfide diffusion is another important factor for consideration. The loading of LGPS in the CNT/LGPS cells is 1.5 mg cm^{-2} unless otherwise specified.

To explore the stability of LGPS during cycling, the electrochemical impedance spectroscopy (EIS) analysis was conducted. As shown in Fig. 4d and S23,† the addition of LGPS lowered the charge transfer resistance and catholyte resistance consistently through 100 cycles, displaying the stable catalytic effect of LGPS. We also conducted XRD measurements on the electrode after cycling to investigate whether the structure of LGPS changed. Even after cycling, the CNT/LGPS electrode retained the peaks of LGPS, as shown in Fig. S24,† indicating that there

was no phase change of LGPS in the liquid electrolyte under the cycling conditions. Under very lean conditions (E/S ratio of 2.9 μL mg^{-1}) with a high sulfur loading of 8.1 mg cm^{-2}, the LGPS cell has a maximum areal capacity of 6.13 mA h cm^{-2} (Fig. 4e). The extremely lean electrolyte condition (2.9 μL mg^{-1}) necessitated 25 cycles for full activation due to the highly concentrated catholyte and additional sulfur. After the activation process, normal operation was observed, showing a capacity retention of 70% at the 135th cycle. The total energy throughputs over 70% capacity retention (135th cycle) and 60% retention (200th cycle), which represent the total amount of energy utilized over the course of the cycling (*i.e.*, the area under the cycling curve in Fig. 4e), are 891 and 665 mA h cm^{-2}, respectively. As displayed in Fig. 4f, these values are high among the reported values in the literature under lean electrolyte conditions (E/S ratio of 2–5 μL mg^{-1} and sulfur loading of 4 mg cm^{-2} or higher), particularly at an extremely low E/S of 2–3 μL mg^{-1}. In fact, a very limited number of papers are available with a lifespan greater than 100 cycles at an E/S ratio of ~3 μL mg^{-1}. The poor cycling performance can be attributed to the aggravated passivation of irreversible solid-state elemental sulfur and Li_2S due to sluggish kinetics on the surface of the CNT host where the liquid–solid phase conversion occurs.[28] The LGPS in this study could offer Li-ion pathways to alleviate the unwanted reactions. Additionally, it is worth mentioning that the N/P ratio in our cells is 2, which is much lower than typical values in the literature as a small N/P ratio is important for increasing the energy density.[64] The energy density of our cell shown in Fig. 4e is 251 W h kg^{-1} at the maximum capacity when the cathode, anode, separator, and electrolyte except for the casing are considered (see details in Note S2, ESI†). The energy density value was calculated based on the actual masses of the components used without assumptions.

Conclusions

In summary, this study demonstrates that LGPS is effective in providing Li-ion pathways and facilitating redox reactions. DFT calculations show the affinity of polysulfides to LGPS, and UV-vis spectra suggest adsorption of polysulfides on LGPS. The polysulfide conversion kinetics have been improved according to the results from the cyclic voltammetry and potentiostatic discharge profiles. The addition of LGPS to the cathode increased the specific capacity as well as rate capability as a result of improved Li-ion diffusion and the conversion rate constant. We found that the conductivity of the solid-state electrolyte needs to be higher than that of catholyte to effectively improve the performance. Another solid-state electrolyte, LLZO whose ionic conductivity is inferior to that of LGPS displayed smaller capacity values and a deeper voltage dip, indicating the sluggish polysulfide conversion reactions. Despite a kinetically harsh condition (E/S ratio of 2.9 μL mg^{-1} and a high sulfur loading of 8.1 mg cm^{-2}), our Li–S batteries with LGPS displayed a high areal capacity of 6.13 mA h cm^{-2} with a capacity retention of 70% at the 135th cycle. These findings highlight the critical role of LGPS in enhancing the performance of Li–S batteries, paving the way for their practical application in energy storage solutions.

Data availability

The data underlying this study are available in the published article and its online ESI.†

Author contributions

Hyunji Park: investigation, software, data curation and writing – original draft. Jooyoung Lee: investigation. Choongho Yu: conceptualization, supervision, writing – review & editing.

Conflicts of interest

There are no conflicts to declare.

References

1 P. G. Bruce, S. A. Freunberger, L. J. Hardwick and J.-M. Tarascon, *Nat. Mater.*, 2012, **11**, 19–29.
2 G. Li, Z. Chen and J. Lu, *Chem*, 2018, **4**, 3–7.
3 X. Liu, J. Q. Huang, Q. Zhang and L. Mai, *Adv. Mater.*, 2017, **29**, 1601759.
4 L. Wang, M. Zhen and Z. Hu, *Chem. Eng. J.*, 2023, **452**, 139344.
5 H. Shi, W. Sun, J. Cao, S. Han, G. Lu, Z. A. Ghazi, X. Zhu, H. Lan and W. Lv, *Adv. Funct. Mater.*, 2023, **33**, 2306933.
6 M. Zhao, B. Q. Li, H. J. Peng, H. Yuan, J. Y. Wei and J. Q. Huang, *Angew. Chem., Int. Ed.*, 2020, **59**, 12636–12652.
7 W. Wang, K. Xi, B. Li, H. Li, S. Liu, J. Wang, H. Zhao, H. Li, A. M. Abdelkader and X. Gao, *Adv. Energy Mater.*, 2022, **12**, 2200160.
8 S. Bai, X. Liu, K. Zhu, S. Wu and H. Zhou, *Nat. Energy*, 2016, **1**, 1–6.
9 H. Chen, Y. Xiao, C. Chen, J. Yang, C. Gao, Y. Chen, J. Wu, Y. Shen, W. Zhang and S. Li, *ACS Appl. Mater. Interfaces*, 2019, **11**, 11459–11465.
10 T. Lei, W. Chen, W. Lv, J. Huang, J. Zhu, J. Chu, C. Yan, C. Wu, Y. Yan and W. He, *Joule*, 2018, **2**, 2091–2104.
11 N. Akhtar, X. Sun, M. Y. Akram, F. Zaman, W. Wang, A. Wang, L. Chen, H. Zhang, Y. Guan and Y. Huang, *J. Energy Chem.*, 2021, **52**, 310–317.
12 C. Cui, R. Zhang, C. Fu, B. Sun, Y. Wang, H. Huo, Y. Ma, Y. Gao, G. Yin and P. Zuo, *Appl. Mater. Today*, 2021, **24**, 101108.
13 P. Wu, M. Dong, J. Tan, D. A. Kang and C. Yu, *Adv. Mater.*, 2021, **33**, 2104246.
14 X. Pu, G. Yang and C. Yu, *J. Electrochem. Soc.*, 2015, **162**, A1396.
15 H. T. Lin, G. Yang, Y.-Y. T. Tsao, Y. Liu and C. Yu, *J. Appl. Electrochem.*, 2018, **48**, 487–494.
16 X. Pu, G. Yang and C. Yu, *Adv. Mater.*, 2014, **26**, 7456–7461.
17 S.-K. Lee, Y. J. Lee and Y.-K. Sun, *J. Power Sources*, 2016, **323**, 174–188.

18 G. Yang, J. Tan, H. Jin, Y. H. Kim, X. Yang, D. H. Son, S. Ahn, H. Zhou and C. Yu, *Adv. Funct. Mater.*, 2018, **28**, 1800595.
19 C. Zhao, G.-L. Xu, Z. Yu, L. Zhang, I. Hwang, Y.-X. Mo, Y. Ren, L. Cheng, C.-J. Sun and Y. Ren, *Nat. Nanotechnol.*, 2021, **16**, 166–173.
20 A. Bhargav, J. He, A. Gupta and A. Manthiram, *Joule*, 2020, **4**, 285–291.
21 T. Cleaver, P. Kovacik, M. Marinescu, T. Zhang and G. Offer, *J. Electrochem. Soc.*, 2017, **165**, A6029.
22 S.-H. Chung and A. Manthiram, *ACS Appl. Mater. Interfaces*, 2018, **10**, 43749–43759.
23 G. Li, W. Lei, D. Luo, Y. Deng, Z. Deng, D. Wang, A. Yu and Z. Chen, *Energy Environ. Sci.*, 2018, **11**, 2372–2381.
24 M. Li, Y. Zhang, Z. Bai, W. W. Liu, T. Liu, J. Gim, G. Jiang, Y. Yuan, D. Luo and K. Feng, *Adv. Mater.*, 2018, **30**, 1804271.
25 H. Wang, B. D. Adams, H. Pan, L. Zhang, K. S. Han, L. Estevez, D. Lu, H. Jia, J. Feng and J. Guo, *Adv. Energy Mater.*, 2018, **8**, 1800590.
26 C. Luo, E. Hu, K. J. Gaskell, X. Fan, T. Gao, C. Cui, S. Ghose, X.-Q. Yang and C. Wang, *Proc. Natl. Acad. Sci. U. S. A.*, 2020, **117**, 14712–14720.
27 Y. Tsao, H. Gong, S. Chen, G. Chen, Y. Liu, T. Z. Gao, Y. Cui and Z. Bao, *Adv. Energy Mater.*, 2021, **11**, 2101449.
28 H. Pan, K. S. Han, M. H. Engelhard, R. Cao, J. Chen, J. G. Zhang, K. T. Mueller, Y. Shao and J. Liu, *Adv. Funct. Mater.*, 2018, **28**, 1707234.
29 F. Y. Fan and Y.-M. Chiang, *J. Electrochem. Soc.*, 2017, **164**, A917.
30 S. Chen, Y. Gao, Z. Yu, M. L. Gordin, J. Song and D. Wang, *Nano Energy*, 2017, **31**, 418–423.
31 Y. Ren and A. Manthiram, *Adv. Energy Mater.*, 2022, **12**, 2202566.
32 A. Elabd, J. Kim, D. Sethio, S. Kang, T. Kang, J. W. Choi and A. Coskun, *ACS Energy Lett.*, 2022, **7**, 2459–2468.
33 X. Liu, T. Qian, J. Liu, J. Tian, L. Zhang and C. Yan, *Small*, 2018, **14**, 1801536.
34 H. Chen, Z. Wu, M. Zheng, T. Liu, C. Yan, J. Lu and S. Zhang, *Mater. Today*, 2022, **52**, 364–388.
35 L. Wang, W. Hua, X. Wan, Z. Feng, Z. Hu, H. Li, J. Niu, L. Wang, A. Wang and J. Liu, *Adv. Mater.*, 2022, **34**, 2110279.
36 M. Li, X. Huang, C. C. Su and K. Amine, *J. Am. Chem. Soc.*, 2024, **146**, 23182–23193.
37 Z.-X. Chen, Q. Cheng, X.-Y. Li, Z. Li, Y.-W. Song, F. Sun, M. Zhao, X.-Q. Zhang, B.-Q. Li and J.-Q. Huang, *J. Am. Chem. Soc.*, 2023, **145**, 16449–16457.
38 Q. Cheng, Z. X. Chen, X. Y. Li, C. X. Bi, F. Sun, X. Q. Zhang, X. Ma, B. Q. Li and J. Q. Huang, *Adv. Energy Mater.*, 2023, **13**, 2301770.
39 J. Chen, X. Geng, C. Wang, X. Hou, H. Wang, Q. Rong, N. Sun, W. Liu, L. Hu and X. Fu, *J. Mater. Chem. A*, 2024, **12**, 11038–11048.
40 Q. Jin, X. Qi, F. Yang, R. Jiang, Y. Xie, L. Qie and Y. Huang, *Energy Storage Mater.*, 2021, **38**, 255–261.
41 Z. Han, S. Li, M. Sun, R. He, W. Zhong, C. Yu, S. Cheng and J. Xie, *J. Energy Chem.*, 2022, **68**, 752–761.
42 Z. Han, S. Li, Y. Wu, C. Yu, S. Cheng and J. Xie, *J. Mater. Chem. A*, 2021, **9**, 24215–24240.
43 G. Zhou, H. Chen and Y. Cui, *Nat. Energy*, 2022, **7**, 312–319.
44 N. Kamaya, K. Homma, Y. Yamakawa, M. Hirayama, R. Kanno, M. Yonemura, T. Kamiyama, Y. Kato, S. Hama and K. Kawamoto, *Nat. Mater.*, 2011, **10**, 682–686.
45 Q. Pang, X. Liang, C. Y. Kwok and L. F. Nazar, *Nat. Energy*, 2016, **1**, 1–11.
46 C. Chang and X. Pu, *Nanoscale*, 2019, **11**, 21595–21621.
47 L. Cheng, L. A. Curtiss, K. R. Zavadil, A. A. Gewirth, Y. Shao and K. G. Gallagher, *ACS Energy Lett.*, 2016, **1**, 503–509.
48 X. Wang, L. Ye, C.-W. Nan and X. Li, *ACS Appl. Mater. Interfaces*, 2022, **14**, 46627–46634.
49 A. Bhandari and J. Bhattacharya, *J. Phys. Chem. C*, 2016, **120**, 29002–29010.
50 Y. Mo, S. P. Ong and G. Ceder, *Chem. Mater.*, 2012, **24**, 15–17.
51 Y.-H. Wang, J. Yue, W.-P. Wang, W.-P. Chen, Y. Zhang, Y.-G. Yang, J. Zhang, Y.-X. Yin, X. Zhang and S. Xin, *Mater. Chem. Front.*, 2021, **5**, 5328–5335.
52 R. Prasada Rao and S. Adams, *J. Mater. Sci.*, 2016, **51**, 5556–5564.
53 H. Wan, S. Liu, T. Deng, J. Xu, J. Zhang, X. He, X. Ji, X. Yao and C. Wang, *ACS Energy Lett.*, 2021, **6**, 862–868.
54 X. Lin, W. Li, X. Pan, S. Wang and Z. Fan, *Batteries*, 2022, **9**, 14.
55 W. Hua, H. Li, C. Pei, J. Xia, Y. Sun, C. Zhang, W. Lv, Y. Tao, Y. Jiao and B. Zhang, *Adv. Mater.*, 2021, **33**, 2101006.
56 C. Li, W. Ge, S. Qi, L. Zhu, R. Huang, M. Zhao, Y. Qian and L. Xu, *Adv. Energy Mater.*, 2022, **12**, 2103915.
57 C. Luo, X. Liang, Y. Sun, W. Lv, Y. Sun, Z. Lu, W. Hua, H. Yang, R. Wang and C. Yan, *Energy Storage Mater.*, 2020, **33**, 290–297.
58 Y. Li, W. Wang, B. Zhang, L. Fu, M. Wan, G. Li, Z. Cai, S. Tu, X. Duan and Z. W. Seh, *Nano Lett.*, 2021, **21**, 6656–6663.
59 F. Y. Fan, W. C. Carter and Y. M. Chiang, *Adv. Mater.*, 2015, **27**, 5203–5209.
60 L. C. Gerber, P. D. Frischmann, F. Y. Fan, S. E. Doris, X. Qu, A. M. Scheuermann, K. Persson, Y.-M. Chiang and B. A. Helms, *Nano Lett.*, 2016, **16**, 549–554.
61 L. Li, T. A. Pascal, J. G. Connell, F. Y. Fan, S. M. Meckler, L. Ma, Y.-M. Chiang, D. Prendergast and B. A. Helms, *Nat. Commun.*, 2017, **8**, 2277.
62 Y. Li, J.-T. Han, C.-A. Wang, H. Xie and J. B. Goodenough, *J. Mater. Chem.*, 2012, **22**, 15357–15361.
63 Y. Wang, P. Yan, J. Xiao, X. Lu, J.-G. Zhang and V. L. Sprenkle, *Solid State Ionics*, 2016, **294**, 108–115.
64 F. Shi, L. Zhai, Q. Liu, J. Yu, S. P. Lau, B. Y. Xia and Z.-L. Xu, *J. Energy Chem.*, 2022, **76**, 127–145.